## Supplementary information

# Three-Dimensional and Chemical Mapping of Intracellular Signalling Nanodomains in Health and Disease with Enhanced Expansion Microscopy

Thomas M. D. Sheard[1], Miriam E. Hurley[1], John Colyer[1], Ed White[1], Ruth Norman[1], Eleftheria Pervolaraki[1], Kaarjel K. Narayanasamy[1], Yufeng Hou[2], Hannah M. Kirton[1], Zhaokang Yang[1], Liam Hunter[3], Jung-uk Shim[3], Alexander H. Clowsley[4], Andrew J. Smith[1], David Baddeley[5], Christian Soeller[4], Michael A. Colman[1], and Izzy Jayasinghe[1,*]

1. School of Biomedical Sciences, Faculty of Biological Sciences, University of Leeds, Leeds LS2 9JT, UK.
2. Institute of Experimental Medical Research, Oslo University Hospital Ullevål, Oslo, Norway.
3. School of Physics and Astronomy, Faculty of Mathematics and Physical Sciences, University of Leeds, Leeds, LS2 9JT, UK.
4. Living Systems Institute, University of Exeter, Devon, EX4 4QL, UK.
5. Auckland Bioengineering Institute, University of Auckland, Auckland, New Zealand.

* Correspondence to Izzy Jayasinghe *via* I.Jayasinghe@leeds.ac.uk

## Supplemental experimental procedures

### *Cell preparation and animal models*

All experiments were performed according to the UK Animals (Scientific Procedures) Act of 1986 with approval of the UK Home Office. Adult male Wistar rats, aged ~ 5 weeks (200 g) were given either an intraperitoneal injection of saline or crotaline (MCT, Sigma-Aldrich) at a dose of 60 mg per kg of body weight to induce pulmonary arterial hypertension (PAH) as detailed previously.[1] Between days 21 and 28, the MCT administered animals were monitored for signs of right ventricular failure (weight loss, cold extremities, piloerection, lethargy and dyspnoea). Animals were concussed with a blow to the head and euthanized by cervical dislocation. Hearts were briefly excised, cannulated at the aorta onto a flow-controlled Langendorff perfusion system. The hearts were perfused for 5 mins with Tyrode's solution consisting of (in mM): NaCl: 130, $MgCl_2$: 1.4, KCl: 5.4, $NaH_2PO_4$: 0.4, HEPES: 5, Glucose: 10, taurine: 20 and $CaCl_2$: 0.75 at pH 7.4 and 37°C. Tyrode's solution containing $CaCl_2$: 0, EGTA (Sigma): 0.1, Collagenase-II (Worthington Biochemicals, USA): 1 mg/mL and protease (Sigma) 0.08 mg/mL was then delivered for ~ 8 mins to digest the cardiac tissue.[2] Ventricles were dissected, diced and triturated to liberate ventricular myocytes. In experiments comparing right ventricular cells from MCT administered animals (MCT-RV) with control, the right and left ventricles were dissected separately prior to isolation of cell suspensions. Cell suspensions were washed in fresh Tyrode's solution and adhered to laminin-coated coverslips attached to acrylic imaging chambers according to the protocol detailed previously.[3] Once attached, cells were fixed *in situ* with 2% paraformaldehyde (PFA; Sigma) (w/v) in phosphate-buffered saline (PBS, Sigma) at room temperature (RT) for ten minutes. Cells were stored in fixed cell storage solution (0.1% sodium azide ($NaN_3$, Sigma), 5% bovine serum albumin (BSA, ThermoFisher, UK) until immunostaining.

In experiments observing differences with enhanced β-adrenergic stimulation, isolated ventricular cells were adhered to coverslips for 2 hours, then stimulated with electrical field stimuli at 1 Hz 10 mins while undergoing perfusion with Tyrode's containing 100 nM Isoproterenol (Sigma). Cells were fixed *in situ* with 2% PFA in PBS at RT.

### *Immunofluorescence labelling and antibodies*

Cells were permeabilised with 0.1% or 1% Triton X-100 (Sigma) in PBS for 10 mins, blocked with 10% normal goat serum (NGS, ThermoFisher) in PBS for one hour. Antibodies (Abs) were diluted and applied to the cell samples in the incubation buffer containing (in w/v or v/v) 0.05% $NaN_3$; 2% BSA; 2% NGS; 0.05% Triton X-100 dissolved in PBS. Cells were incubated in primary and secondary Abs overnight at 4°C and for 2 hrs at room temperature (RT) respectively. Following each Abs incubation step, samples were washed three times in fresh PBS at RT for 10 mins.

Ryanodine receptors were labelled either with a mouse anti-RyR2 IgG (MA3-916; ThermoFisher) or a rabbit anti-RyR2 IgG (HPA020028, Sigma). pSer2808 was labelled with anti-RyR2-pSer2808 IgG (A010-30AP, Badrilla Ltd, UK). Also used, were z-disc marker: mouse anti-α-actinin IgG (GTX29465, GeneTex, UK) and microtubule marker: rabbit-α-tubulin IgG (ab190573, Abcam). Secondary Abs used for ExM included goat anti-mouse IgG and anti-rabbit IgG conjugates of AlexaFluor488 (ThermoFisher) and Janelia Fluor 549. The latter conjugates were prepared by us using unlabelled affinity-purified anti-mouse and anti-rabbit IgG (Jackson Immuno) and the Janelia Fluor 549 SE labelling kits (Janelia HHMI, VA). For DNA-PAINT experiments, anti-mouse and anti-rabbit IgGs were linked to custom-made oligonucleotide 'docking' strands P1 or P3, designed by Jungmann *et al,*[4] and synthesized *via* Eurofins Ltd (UK), using the Thunder-link oligo-Abs conjugation kits (Innova Biosciences, Cambridge) as detailed previously.[3] Complementary P1 and P3 'imager' strands were designed to carry an Atto655 fluorophore and applied to the cell samples during imaging in Buffer C at a concentration of 300 pM. Cells prepared in dSTORM experiments were labelled with anti-mouse IgG conjugates of AlexaFluor680 (ThermoFisher) and mounted within a switching buffer containing 90% (v/v) glycerol and 20 mM cysteamine (Sigma) dissolved in PBS.

*ExM sample preparation*

Cells, following immunofluorescence labelling, were incubated with 0.1 mg/ml Acryloyl-X (AcX, Thermo Fisher) in PBS overnight at 4°C, then washed in PBS immediately prior to addition of gel solution from either the 4x or 10x ExM protocols.

4x ExM (also known as proExM) was performed as previously described.[5] Cells were incubated with the "monomer solution" containing (w/v, sourced from Sigma) 8.6% sodium acrylate (SA), 2.5 % acrylamide; 0.15% N,N'-Methylenebisacrylamide, 11.7% NaCl, PBS, 0.1% Ammonium persulfate (APS) and N,N,N',N'-Tetramethylethylenediamine (TEMED) first for 30 mins at 4°C and then over 2 hrs at 37°C. The gel was polymerised in a sealed acrylic chamber comprising two coverslips, and coverslip spacers. Gels were then ejected from chambers, and subjected to digestion in 0.2 mg/mL proteinase K (ProK, New England Biolabs) dissolved in a "digestion buffer" (50 mM Tris pH 8.0, ThermoFisher; 1mM ethylenediaminetetraacetic acid (EDTA, Sigma); 0.5% Triton X-100; 0.8M guanidine HCl, Sigma; $dH_20$) overnight at RT. Gels were expanded by gentle washing in fresh deionized $H_2O$ ($dH_2O$) until there was no further change in the gel size.

10x ExM preparation was performed as previously described.[6] A gel monomer solution consisted of 4:1 molar ratio of dimethylacrylamide and molecular-grade SA, dissolved in $dH_2O$ saturated in $N_2$ over 1 hr on ice. Potassium persulfate (KPS, Sigma) was added at 0.4% molar relative to monomer concentration from a 0.036 g/ml stock, made fresh for each experiment, and the solution was bubbled for another 15 mins on ice. 500 µl of the gel monomer solution was mixed rapidly with 2 µl of TEMED and quickly added to the cells. Gelation was allowed in a sealed acrylic chamber comprising two coverslips – one each at the base and roof. Gel polymerisation was completed by 48 hrs. Then the gels were extracted carefully from the chambers and subjected to the digestion and gel expansion steps as in the 4x ExM protocol.

## Image acquisition and primary image processing

**Confocal/ Airyscan microscopy:** For imaging ExM samples, the gels were placed within acrylic chambers which were custom-made to fit the stages of the microscopes. The chamber itself was typically square (adapted in size and shape to fit 4x or 10x ExM gels) and consisted of a base made of a glass No. 1.5 coverslip (Menzel Gläser, Germany), custom-coated with 0.1% (v/v) poly-L-lysine (Sigma) in order to retain the gels flush on the coverslip. For confocal and Airyscan imaging an inverted LSM880 with Airyscan (Carl Zeiss, Jena) was used with Plan-Aprochromat 63x 1.4 NA objective with a working distance of 0.19 mm. Alexa Fluor 488 and Janelia Fluor 549 were excited with 488 nm and 561 nm DPSS lasers and emission bands sub-selected using the in-built spectral detector. In confocal mode, emission was recorded *via* an in-built photomultiplier tube placed behind a pinhole set to 0.7 Airy Units. For Airyscan, the emission was recorded with the in-built 32-element GaAsP detector. Pixel sampling of primary data was < 90 and < 40 nm/px for confocal and Airyscan respectively. In the acquisition of 3D z-series, samples were imaged up to a sample depth of 50 µm where possible, however generally no deeper than 20 µm, at step sizes of 150 and 75 nm for confocal and Airyscan imaging. To enhance the signal-to-noise ratio, confocal 3D z-stacks were subjected to a Richardson-Lucy maximum-likelihood deconvolution with ~ 10 iterations, implemented in IDL as detailed previously.[7] Airyscan data were subjected to a pixel-reassignment and a linear Wiener deconvolution *via* the Zen software.

**DNA-PAINT and dSTORM:** Immuno-labelled cells were either retained within custom-made imaging chambers, affixed to coverslip base or mounted between glass slide and coverslip for DNA-PAINT and dSTORM respectively. Samples were imaged on bespoke single-molecule localisation systems consisting of Nikon TE2000 total internal reflection fluorescence (TIRF) microscopes equipped with 60x 1.49 NA TIRF objectives. A 671 nm diode laser (Viasho, China) beam was focused either in oblique (HiLo) configuration[8] for dSTORM in imaging cell interior or at an angle greater than the TIRF critical angle, confirmed by the detection of TIR light at the back focal plane of the objective, for cell surface RyR imaging with DNA-PAINT as described previously in Jayasinghe *et al* supplementary methods.[3] Single molecule emissions were detected with a 5.5 megapixel sCMOS camera (Andor, Belfast) and acquired into time series at 10-20 Hz using the freely-available Python Microscopy Environment (PYME) software (www.python-microscopy.org) which utilises an algorithm which corrects for the non-uniform pixel noise in single molecule image data acquired with sCMOS cameras, described previously.[9] PYME was used for localising the fluorophore positions and rendering the point data of dSTORM and DNA-PAINT experiments onto 5 nm and 1 nm pixel grids for further spatial analyses.

*Spatial analysis of EExM and DNA-PAINT data*

**Segmentation:** Local ensembles of punctate RyR densities were segmented into clusters using an extension of a cluster segmentation protocol which was developed for DNA-PAINT images of RyR clusters in rat ventricular myocytes.[3] Briefly, this involved the calculation of a binary mask with a global threshold set at the intensity value which encapsulated 80% of the integrated intensity for a given image. Within the RyR cluster regions, holes that were smaller than 3000 $nm^2$ in 2D data or smaller than 160,000 $nm^3$ in 3D data were filled in order to obtain a robust segmentation of the RyR cluster area or volume. In the distance-based analysis of phosphorylated RyRs, a Euclidean distance map was constructed within the cluster area of surface nanodomains using the binary masks constructed from the above segmentation.

**Detection:** Punctate labelling densities which were typical for RyR and pSer2808 Ab labelling in EExM and DNA-PAINT data were analysed by their spatial distribution. A detection algorithm, similar to that used previously,[3] was implemented in Python to record the three-dimensional coordinates of the centroid of each punctum. Each centroid was treated as a single RyR. For cell surface (2D) DNA-PAINT and 10x EExM data, the detection was 2D. Analysis of RyRs and pSer2808 labelling in cell interior nanodomains required the application of the detection to 3D data (z-stacks). This analysis included an iterative two-step process. In the first, the image data were smoothed with either a 2D or a 3D Gaussian kernel (in-plane sigma of 14 nm; sigma in the axial dimension of 35 nm) and a threshold applied according to a multi-threshold series to segment regions detected as unitary puncta. In the second step, an adaptive 2D or 3D Gaussian shape was fitted to each region to localise its sub-pixel coordinates, exported as a list for further analysis. As with the previous DNA-PAINT data of RyRs,[3] some variation in the fitted widths of the puncta were observed between puncta (arising most likely from local heterogeneity in the fluorophore density at each RyR), therefore puncta up to the size (FWHM of the fit) of ~ 20 nm, in-plane, were accepted as solitary RyRs. For volumes which were acquired deeper within the sample where the in-plane FWHM of the PSF was larger, this criterion was relaxed up to 25 nm. The centroids were used for determining cluster sizes, analysis of nearest and average neighbour distances and phosphorylation re-assignment to RyRs based on co-localisation with pSer2808 puncta.

To measure the longitudinal separation between the double peaks of α-actinin observed in the DNA-PAINT and 10x EExM images, the sub-pixel centroids of each intensity peak was calculated. This was achieved by fitting Gaussian functions along each horizontal row of pixels as detailed previously.[10, 11] The distance between the two centroids was calculated for each line and an average distance was taken for each dataset (as plotted in Fig 1E).

**Simulation of confocal, dSTORM, DNA-PAINT and EExM images:** The stylised 3D models of the z-disc (supplementary Fig S1) and the curved nanodomains (supplementary Fig S4) were convolved with a PSF that approximated the resolution achieved by each technique. For confocal models, the PSF was estimated by averaging between deconvolved images of 100 nm microspheres. For 4x and 10x EExM, the estimated PSF for Airyscan data was scaled down by the estimated gel expansion factor. dSTORM and DNA-PAINT simulations used the image simulator of PyME detailed previously.[3] For these, image volumes containing the label positions were convolved with a 3D Gaussian PSF with a sigma of 5 nm in-plane and 200 nm axially. To simulate the 2D dSTORM and DNA-PAINT images (of the z-disc labelling of α-actinin, a maximum-intensity projection across a 100 nm depth was taken as the starting template for generating the synthetic images with PyME. The software assigned fluorophore positions throughout the image area in proportion to the local pixel intensity of the template. See Table S2 in previous report[3] for the image simulator parameters used for achieving realistic dSTORM and DNA-PAINT simulations.

**pSer2808 reassignment:** The 3D coordinates of the RyR and pSer2808 labelling puncta were detected independently (in their separate channels of the two-colour data). The RyR punctum which were nearest to the centroid of pSer2808 punctum was marked as an RyR phosphorylated at Ser2808. Only 1 RyR was marked as phosphorylated for a given pSer2808 punctum. RyRs whose centroids were outside of the 30-nm radius from a given pSer2808 were disregarded; pSer2808 puncta which were un-assigned to an RyR punctum was recorded as ‘undetermined’.

### *Simulation of the spatiotemporal $Ca^{2+}$ dynamics*

To demonstrate the potential for the high-resolution structural data to be used in computational modelling studies, preliminary simulations of the spatiotemporal $Ca^{2+}$ dynamics in the nanodomains were performed. Simulations were focussed on illustrating the isolated effects of the changes to the nanodomain layout observed between control and MCT, *i.e.* number and distribution of phosphorylated and non-phosphorylated RyRs, independent from any electrical/dynamical and environmental remodelling which may be observed in disease. Comprehensive analysis was beyond the scope of the present study, and therefore simulations were performed using a general implementation of model dynamics and over a range of parameters to avoid parameter-specific interpretation.

Multiple previous studies have simulated spatiotemporal $Ca^{2+}$ dynamics in individual nanondomains,[12-15] in general solving the diffusion of $Ca^{2+}$ in the nanodomain at a spatial resolution of ~1 RyR corresponding to ~40 nm. To fully utilise the structural data acquired in this study, $Ca^{2+}$ diffusion was solved on 2D grids discretised at a resolution of 10 nm: Selected reconstructions of flat nanodomains from control and MCT, representative from the median in size and RyR number, were down-sampled to 10 nm and embedded in a 2D grid 100 nm larger in $x$ and $y$. The 2D sheet comprises two regions – the segmented nanodomain itself (within which all the RyRs are found as point sources) and the surrounding intracellular space. $Ca^{2+}$ dynamics within this grid are described by the reaction-diffusion equation (Eq 1).

$$\boxed{\frac{dCa^{2+}}{dt} = \nabla^2 Ca^{2+} + \varphi} \tag{Eq 1}$$

Where $\varphi$ is a local reaction term defined by the L-type $Ca^{2+}$ channel and/or RyR flux (described below), and $\boxed{\nabla^2}$ is the spatial Laplacian operator in 2D. The spatial derivative was solved using the isotropic Finite Differences Method and the solution was advanced in time using the forward-Euler method. The edges of the grid were connected to an infinite pool representing the bulk intracellular space. Simulations were performed for the first 50 ms of cardiac EC coupling.

To represent $Ca^{2+}$ influx due to L-type $Ca^{2+}$ channel activation associated with cardiac excitation, an idealised triangular waveform was used to apply a flux homogeneously to the region segmented as the nanodomain 10 ms after the start of the simulation, increasing the average $Ca^{2+}$ concentration to 5-10 μM (dependent on nanodomain size and the peak magnitude of the $Ca^{2+}$ flux) described by equation (Eq 2):

$$\boxed{J_{LTCC} = g_{LTCC}\left(1 + e^{-(t-10)/0.283}\right)^{-1}.\,0.5\left(1 + e^{(t-13)/4.721}\right)^{-1}} \qquad \text{(Eq 2)}$$

Parameter values are given in supplementary table 1.

RyR dynamics, controlling intracellular calcium release, were described through a simple 2-state model (Eq 3), using an approach similar to a simplified version of that presented by.[16]. Note that the symbol 'O' in Eq 3 represents the open probability, not a zero, in keeping with the conventions of Markov chain model descriptions.

$$\boxed{J_{rel} = g_{RyR}.\,O.\,(Ca_{JSR}^{2+} - Ca^{2+})} \qquad \text{(Eq 3)}$$

$$\boxed{\frac{dO}{dt} = \alpha(1 - O) - \beta O}$$

$$\boxed{\alpha = f\left(Ca^{2+}, Ca_{JSR}^{2+}\right) = A[Ca^{2+}]^{2.5}\left(0.75/\left(1 + e^{-([Ca_{JSR}^{2+}]-400)/50}\right) + 0.25\right)}$$

Each individual RyR can either be in the open (O = 1) or closed (O = 0) state, with the open state the only one in which $J_{\mathrm{rel}}$ is non-zero. The Monte-Carlo method was applied to describe the stochastic state occupancy of individual RyRs. The original *in vitro* study examining the effects of RyR gating kinetics following non-specific phosphorylation of RyRs by Protein Kinase A reported an increase in the RyR open probability by up to a factor of 3.5.[17] To capture an approximate effect of Ser2808-specific phosphorylation in our simulation, the phosphorylated state of the RyR channel was modelled as an increase in the $Ca^{2+}$ sensitivity of the RyRs, multiplying $\alpha$ by a factor between 1.5 and 3 compared to the baseline (which itself was varied), accounting for the likely minimum and maximum potential effects occurring physiologically; phosphorylation sites were given either by the imaging data, or assigned randomly according to the spatial distributions. The junctional sarcoplasmic reticulum (JSR; *i.e.* the region of the endoplasmic reticulum which harbours the RyR cluster) was considered as a homogeneous space, coupled to an infinite pool of the network sarcoplasmic reticulum (NSR; *i.e.* the network portions of the endoplasmic reticulum compartment which connect and buffer the luminal $[Ca^{2+}]$ in the JSR) (Eq 4):

$$\boxed{\frac{dCa_{JSR}^{2+}}{dt} = -J_{rel}^{tot} + J_{NSR}} \qquad \text{(Eq 4)}$$

$$\boxed{J_{NSR} = (800 - Ca_{JSR}^{2+})/\tau_{nsr\_jsr}}$$

Simulations were performed over a range of parameters, 10 simulations per condition, with the behaviour of the different geometries and with/without phosphorylation compared under consistent parameter conditions. Spatial data were output every 0.1 ms for spatiotemporal super-resolution analysis.

The results presented occurred in the middle of the investigated parameter ranges: at low RyR sensitivities and/or LTCC flux, CICR could not be robustly recreated in either control or MCT; at larger RyR sensitivities and/or LTCC flux, CICR could be robustly recreated for all models with and without phosphorylation; within this range, the effect of nanodomain structure (including phosphorylation sites) had a larger impact on the ability to induce CICR and difference between control and MCT were observed, as discussed in the main manuscript.

## Supplementary tables

| **Parameter** | **Symbol** | **Value range (unit)** |
|---|---|---|
| LTCC maximal flux | $g_{\mathrm{LTCC}}$ | 30-100 (μM.ms$^{-1}$) |
| RyR maximal flux | $g_{\mathrm{RyR}}$ | 1 ×10$^{-4}$ - 5 ×10$^{-3}$ (μm$^{3}$.ms$^{-1}$) |
| RyR maximal open rate | $A$ | 0.5-2 × 10$^{-4}$ (μM$^{2.5}$.ms$^{-1}$) |
| RyR closing rate | $\beta$ | 1 (ms$^{-1}$) |
| Time-constant SR filling | $\tau_{\mathrm{nsr\_jsr}}$ | 5 (ms) |

**Supplementary table S1: Model parameter value ranges**

## Supplementary figures

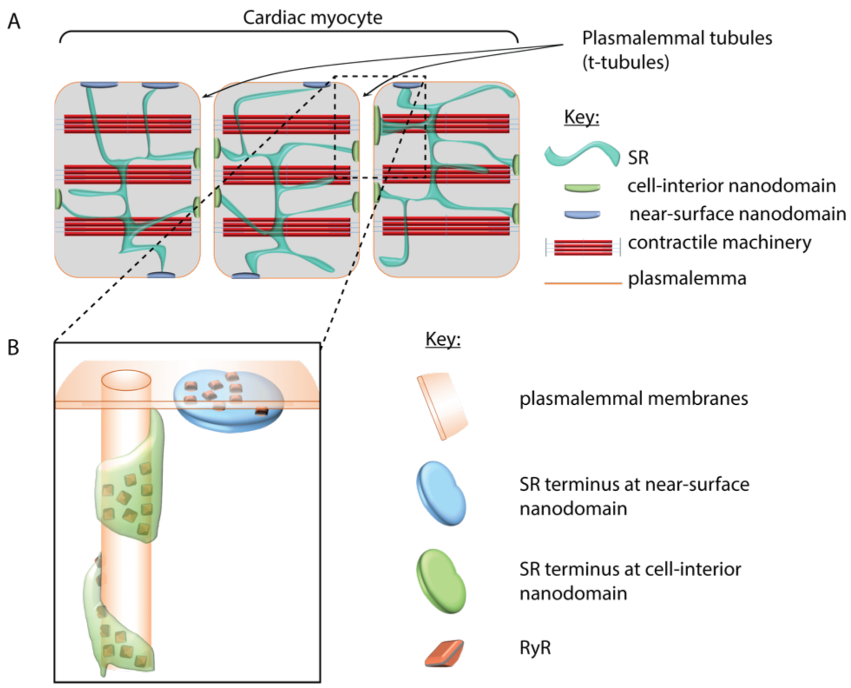

**Supplementary figure S1. Schematic diagram of the locations and topology of near-surface and cell-interior nanodomains.** (A) Schematic of the cardiac myocyte structure illustrates the plasmalemmal tubular (t-tubule) network which spans throughout the deeper regions of the cell. The nanodomains form intimate cytoplasmic interfaces between the sarcoplasmic-endoplasmic reticulum (SR) and the plasmalemmal membranes. A large proportion of the cell's cytoplasm is occupied by the bundles of contractile proteins which allow the cell to contract and power the heartbeat. The filamentous actin of these bundles are anchored by α-actinin at the z-disc (not shown in the schematic), which is located adjacent to the t-tubular invaginations. (B) The termini of the SR which harbour the RyR channels (orange) within the nanodomain therefore form flattened membrane structures either near the cell surface (light blue) or wrapping around the t-tubule membrane invaginations. The latter topology therefore cause the RyRs to be organised in a curved geometry along the t-tubular membrane.

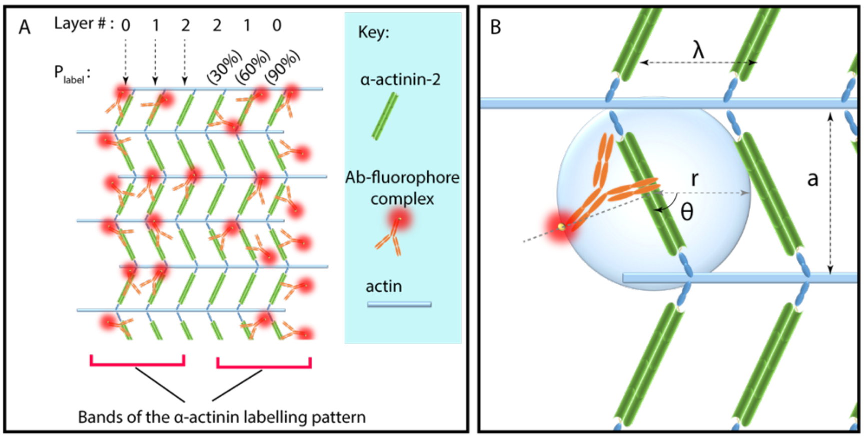

**Supplementary figure S2. Model used for the simulation of the α-actinin organisation in the cardiac z-disc.** (A) Ab binding to z-discs consisting of 6 layers of α-actinin was simulated such that the binding efficiency, limited by steric hinderance to Ab penetration, at the outer-most layers (0) was 90%, intermediate (1) was 60% and inner-most (2) was 30%. The positions of the two bands of the observed labelling pattern (red square brackets) observed with DNA-PAINT and 10x EExM (Fig 1 D) coincide with these gradients of the Ab labelling across the z-disc. (B) The longitudinal spacings between α-actinin targets (λ) was 19 nm as deduced previously,[18] and transverse spacing (a) was 10 nm.[19] The full width of the z-disc was therefore set to 95 nm. Ab binding to α-actinin targets was allowed at a uniformly random angle of θ; the fluorophore localised at a random displacement of r = 10 nm from the α-actinin target to reflect the spatial offset introduced by the Ab. The transverse dimensions of the z-disc were 300 x 300 nm.

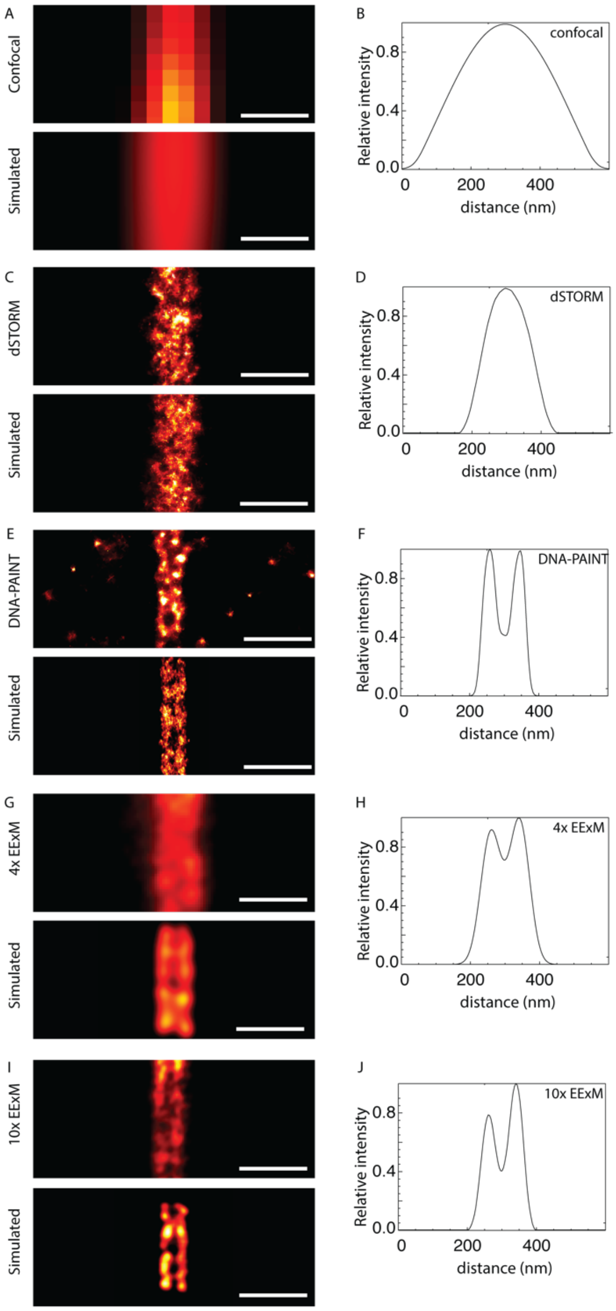

**Supplementary figure S3. Simulation of the double layer morphology of α-actinin Ab labelling in the cardiac z-disc.** Shown, are the morphologies of the α-actinin images either mapped experimentally (upper panels) or simulated with this model (lower) for (A) confocal, (C) dSTORM implemented in HiLo illumination, (E) DNA-PAINT implemented in TIRF (G) 4x EExM and (I) 10x EExM. dSTORM and DNA-PAINT images were simulated using the Python Microscopy Environment open-source software according to a protocol outlined previously [3]. The confocal image was simulated by convolving the model by an experimentally-measured point spread function (PSF). For simulating 4x and 10x EExM, the model volumes were convolved by a scaled version of the Airyscan PSF which was estimated by imaging 50 nm beads with the Zeiss Airyscan 880 GaAsP detector and analysing it with the pixel re-assignment algorithm. The Airysan PSF was scaled down by factors of either 4 or 10 to approximate the effective PSF for 4x and 10x EExM. (B, D, F, H, J) illustrate the respective intensity profiles plotted across the width of the z-disc images simulated with the model, normalized to the peak intensity. Similar to experimentally observed intensity profiles (Fig 1 D), DNA-PAINT, 4x and 10x EExM show clear evidence of the double-layer morphology of α-actinin arising from the trans-z-disc gradient of Ab labelling, with a peak separation of 70-80 nm. Scale bars: 400 nm.

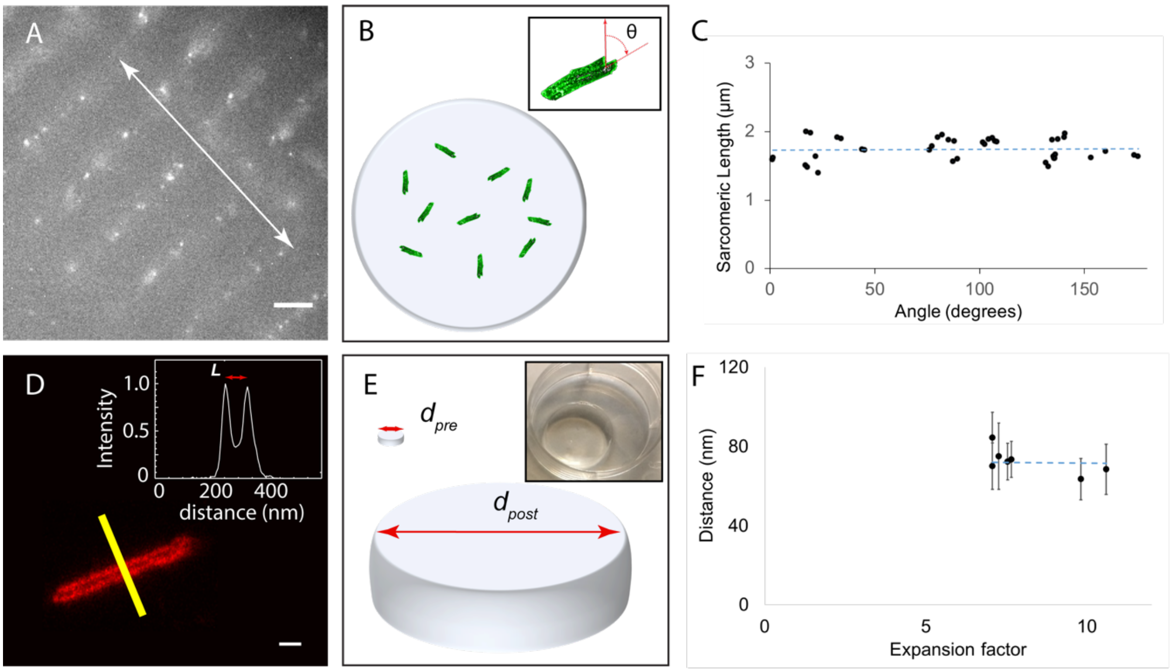

**Supplementary figure S4. Evaluation of consistency in spatial measurements made with EExM on enzymatically-isolated cardiomyocytes.** To ascertain whether the expansion of the cellular structures were directionally isotropic, the average sarcomere length of myocytes expanded within the gels were examined. (A) This was achieved by dividing the longitudinal spacings of 5 z-line bandings of α-actinin or ryanodine receptor staining by 4. (B) Myocytes from different locations of a single, intact, expanded gel were recorded for plotting the average sarcomere length against their relative angle (θ in inset). (C) Scatter plot of measurements from 40 cells revealed that the measured sarcomere length was independent of the angle considered and was approximately Normally distributed with a standard deviation of 0.16 µm, < 10% of the measured average sarcomere length. (D) To establish whether the measurements made with the 10x EEM protocol was sensitive to gel-to-gel variation in the expansion factor, the estimated separation between the α-actinin double-peaks were examined using intensity profiles taken orthogonally to the z-discs (L in inset). (E) The linear (average one dimensional) expansion factor was estimated as $d_{post}/d_{pre}$ where $d_{pre}$ was the average diameter of the gel prior to expansion and $d_{post}$ was the average diameter following expansion (inset shows photograph of a typical disk-shaped gel following expansion). (F) Plot of the estimated mean distance between the α-actinin double-peaks as a function of the expansion factor varying between ~ 6.5x and 10.5x revealed that the measured distances were independent of the gel expansion factor under the experimental conditions used. The error bars indicate the standard deviation of the measurements from each gel (n = 5 cells for each gel).Scale bars: A:1.25 µm, B: 100 nm.

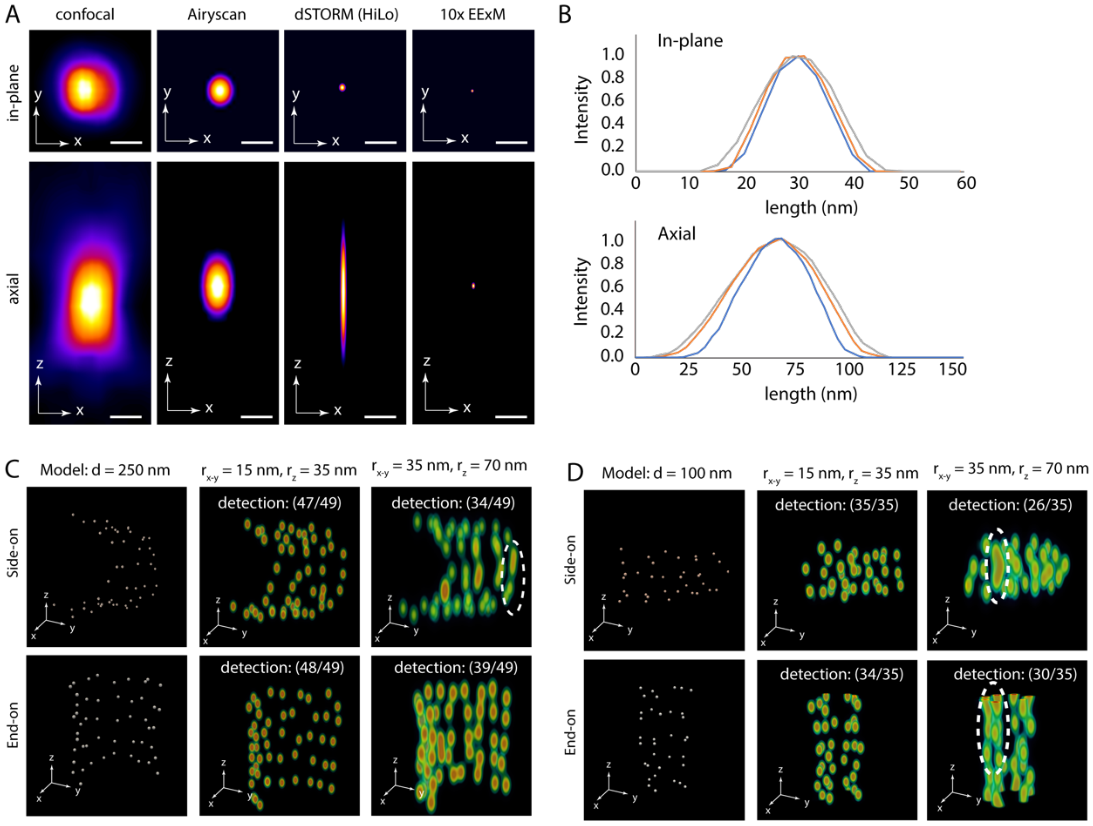

**Supplementary figure S5. Estimation of the effective point spread function and simulation of RyR arrays in interior (curved) nanodomains under imaging conditions of 10x EExM.** (A) Comparison of the estimated point spread functions for confocal, Airyscan, dSTORM (based on widefield detection under HiLo illumination) and 10x EExM. (B) In-plane (upper) and axial (lower) normalise line intensity profiles through 3D Airyscan images of fluorescent beads embedded at depths of 5 µm (blue), 30 µm (orange) and 47 µm (grey) revealed the change in the PSF width from the surface of the gel to the maximum sample depths at which EExM imaging was performed. The length scale shown is adjusted to reflect PSF dimensions of a 10x EExM experiment. (C) 3D volume-rendering (in perspective view) of a model nanodomain with a diameter of curvature (*d*) of 250 nm consisting of RyR positions (white spheroids in model on left) was used to simulate the 3D 10x EExM (middle panels) and 4x EExM (Right) images by convolution with an estimated PSF. The estimated in-plane resolution $r_{x\text{-}y}$ and axial resolution $r_z$ of each image are shown above each panel. (D) Shown as a comparison is an equivalent model of a narrower nanodomain (*d* =100 nm). For each model, the nanodomain orientation relative to the imaging plane – side-on and end-on – were examined for their interaction with the asymmetry of the PSF. The punctate densities of labelling were subjected to the 3D detection protocol used for experimental data; the detection success-rate is shown in each panel. It was observed that 10x EExM localised nearly all the puncta within 15 nm of the original RyR positions. Lower success rate in 4x EExM showed regions (dashed lines) where puncta could not be resolved due to poor axial separation in the simulated image. Scale bars in A: 250 nm

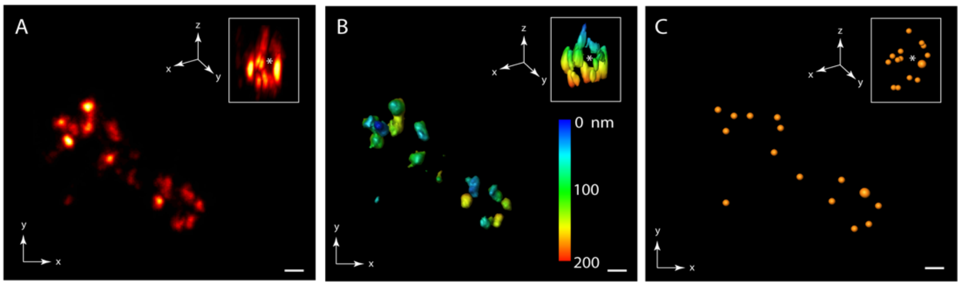

**Supplementary figure S6. Visualisation and detection of 3D localisations of RyRs in cell interior.** (A) The 3D organisation of punctate RyR densities of a single nanodomain wrapping around a cylindrical membrane tubule; seen in 10x EExM volumes (main panel shows a maximum intensity projection of in-plane view; orthogonal view in inset illustrates the hollow centre of the membrane tubule as *); (B) An isosurface 3D visualisation of this 3D data with nanometre-scale depth-coded colour table (scale in nm); (C) The 3D positions of the puncta (represented by spheres) were computationally localised to their individual centroids. Scale bars: 30 nm

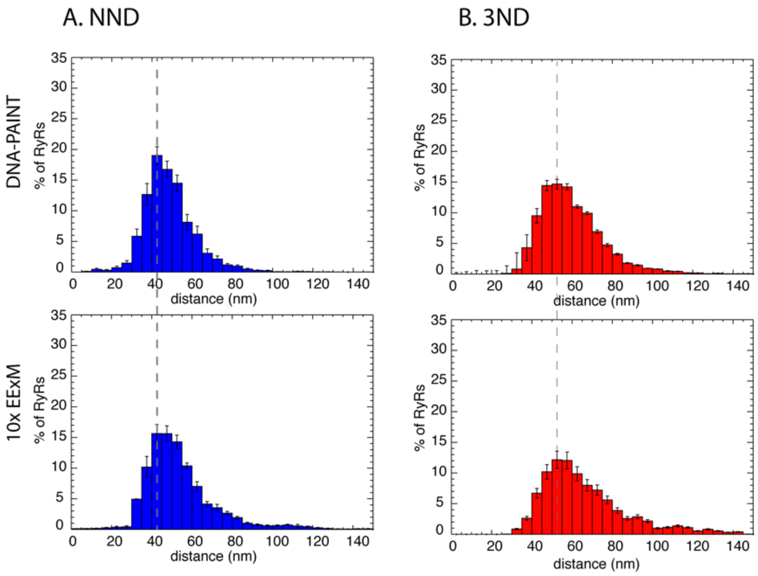

**Supplementary figure S7. Comparison of (A) NND and (B) 3ND measurements made on sub-surface nanodomains of healthy ventricular myocytes with DNA-PAINT (upper) and 10x EExM (lower).** In nanodomains containing >4 RyRs, the NND for each RyR(red) and their average distance to each of the three nearest neighbouring RyRs (3ND; red) were analysed using histograms. The mean NND for DNA-PAINT and 10x EExM data, shown in panel A, were similar (mean ± SD: 40.0 ± 4.7 nm vs 42.04 ± 4.8 nm respectively; Student's t-test p = 0.34; df = 17). There was also no statistically-significant difference between the DNA-PAINT and 10x EExM measurements of the 3ND (mean ± SD: 60.1 ± 8.5 nm vs 64.5 ± 9.6 nm respectively; Mann-Whitney test p = 0.24; df = 17) in panel B. For each histogram analysis (NND and 3ND), the measurements from DNA-PAINT and 10x EExM shared common modes. Whilst a longer rightward tail was observed for 10x EExM data (accounting for < 5% of RyRs analysed), these could reflect smaller populations of RyR which were detected differentially between the two modalities. The dashed lines in each panels indicate the mean measurement made with DNA-PAINT, shown as a guide to the closeness of the alignment of the 10x EExM histograms.

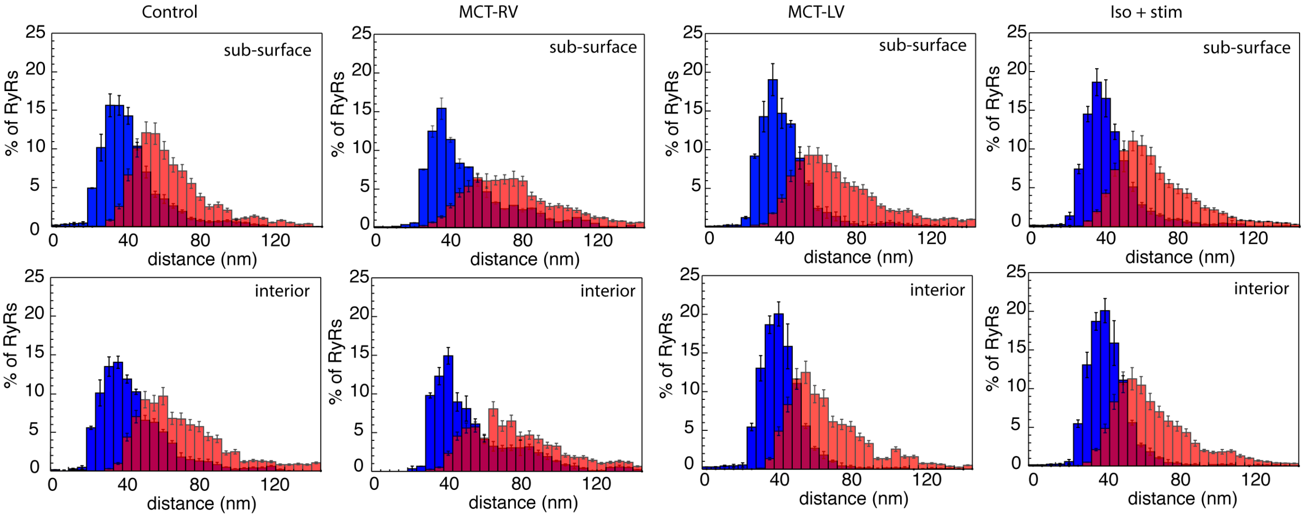

**Supplementary figure S8. NND (blue) and 3ND (red) histograms of RyRs in near-surface (upper row of panels) and interior (lower) nanodomains of rat cardiac muscle cells in control, MCT-RV, MCT-LV and stimulated samples.**

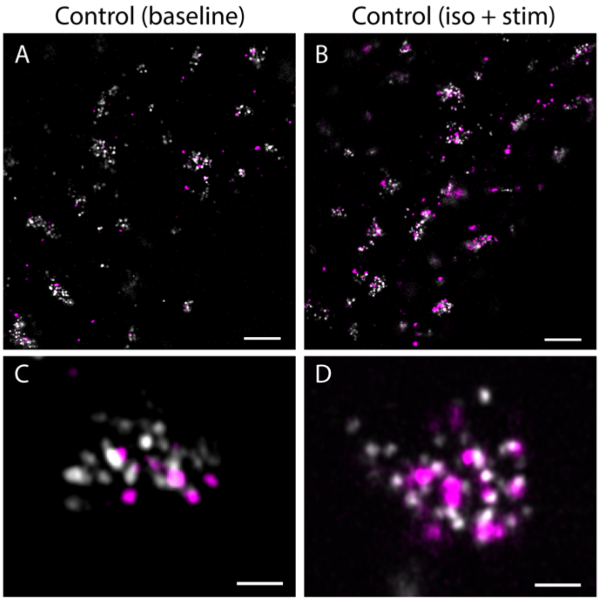

**Supplementary figure S9. 10x EExM visualisation of the increase in Ser2808-specific RyR phosphorylation following stimulation of control ventricular myocytes with Isoproterenol (Iso) and electrical pacing (stim).** (A) Sub-surface RyR labelling (grey) overlaid with pSer2808 (purple) in unstimulated control samples and (B) in cell stimulated with Iso and electrical pacing prior to fixation. Magnified views of individual clusters of (C) unstimulated and (D) stimulated cells are shown. Scale bars: A&B: 500 nm, C&D: 50 nm.

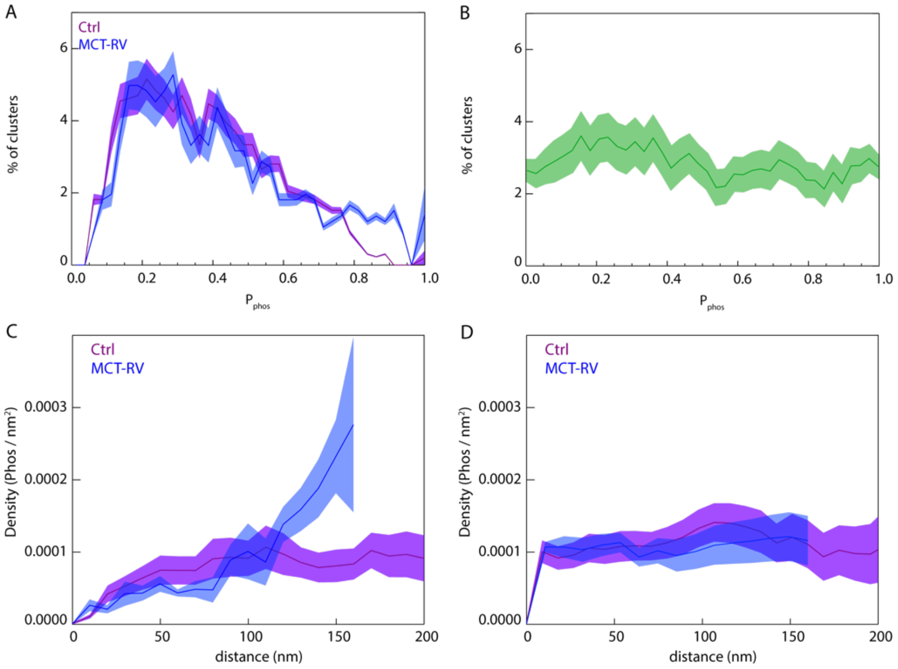

**Supplementary figure S10.** (A) Experimentally-estimated percentage histograms of cluster-specific $P_{phos}$ in the near-surface nanodomains of control and MCT-RV cells. (B) To simulate the distribution expected when $P_{phos}$ in conditions where every RyR cluster has a uniform probability of phosphorylation at Ser2808, experimentally mapped RyR positions were assigned phosphorylation identities according to a random uniform distribution. The dark green line histogram shows the mean percentage of clusters exhibiting a given $P_{phos}$ (bin-size = 0.05). The light-green band reports SEM (n = 9 datasets). The expected percentage histograms of cluster-specific $P_{phos}$ when the RyRs were randomly assigned phosphorylation at Ser2808. (C) Histograms of the 2D experimentally-determined pSer2808 localisation density as a function of the distance within the near-surface nanodomain relative to its boundary in control (purple line) and MCT-RV (blue) cells. (D) Equivalent density histograms when the pSer2808 were randomly assigned to RyRs in the experimentally-mapped RyR maps for control (purple) and MCT-RV clusters (blue).

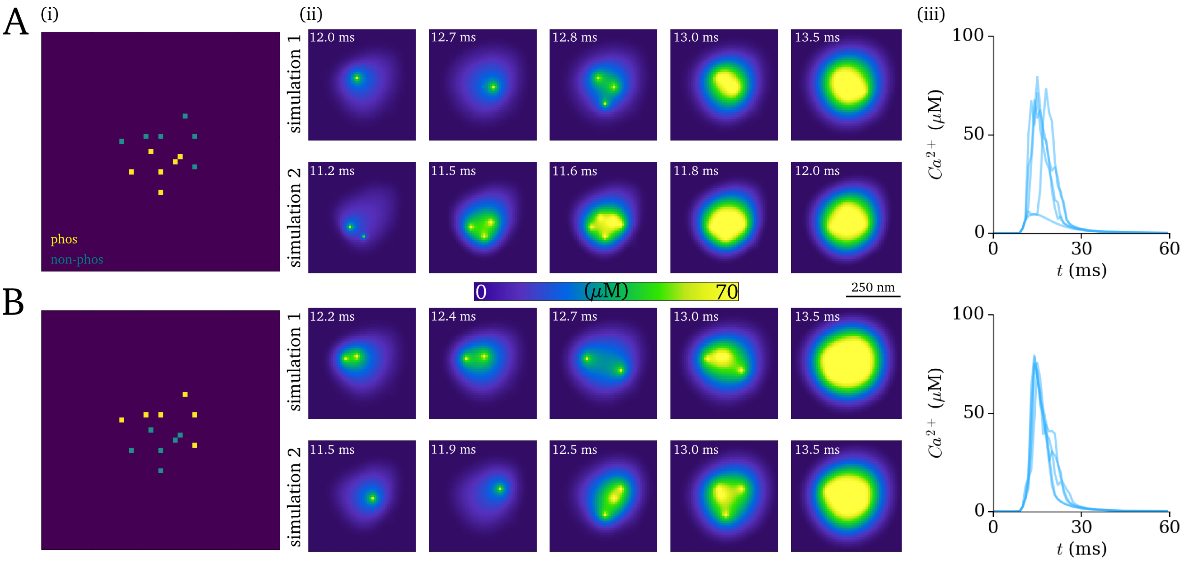

**Supplementary figure S11. Effect of RyR-Ser2808 phosphorylation pattern on excitability.** (i) Compared, are the phosphorylated RyR (yellow) and dephosphorylated RyR (green) pattern from experimentally mapped nanodomain of a control rat ventricular myocyte (A) and its inverse phosphorylation pattern (B). (ii) Two independent simulations of the $Ca^{2+}$ release pattern for each scenario show that the initial $Ca^{2+}$ release activity coincides with the sub-domain containing pSer2808. *i.e.* RyRs on the lower-left of the cluster in the experimental cluster and the RyRs on the upper right in the inversed scenario. (iii) A series of local $Ca^{2+}$ sparks, over-plotted as the time course of the local change in cytoplasmic $Ca^{2+}$ concentration shows that the latter scenario provides the nanodomain with greater consistency in evoking $Ca^{2+}$ sparks.

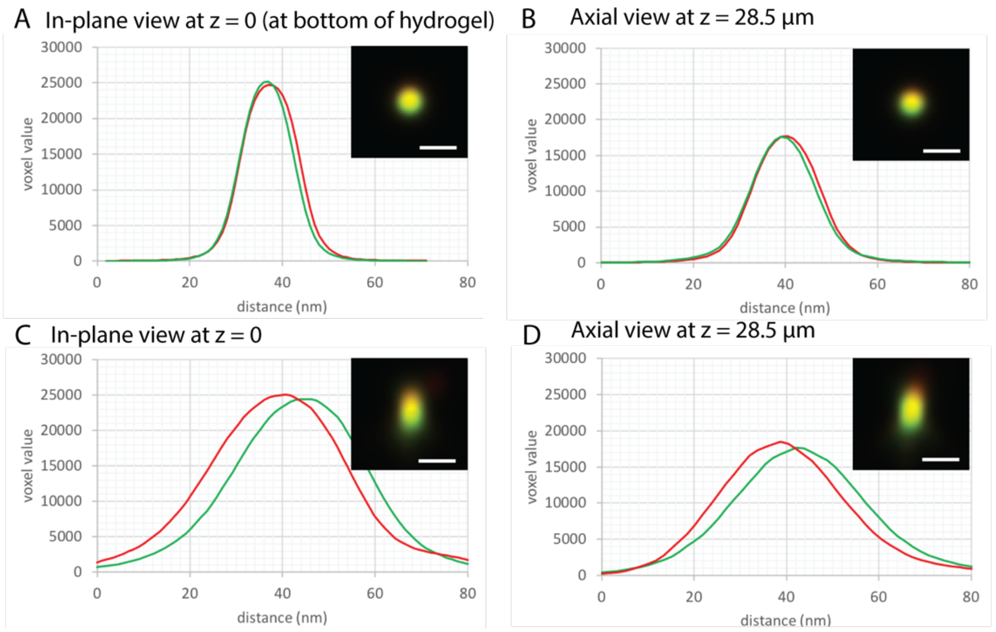

**Supplementary figure S12. Estimation of the chromatic alignment of the point spread function with the 10x EExM imaging method.** Compared in the upper panels, are in-plane and axial line-intensity profiles of the Airyscan images of individual 100-nm TetraSpeck multi-emission beads acquired through the green (equivalent to Alexa488 emission) and red (JaneliaFluor549) emission bands at sample depths of 0 µm (panel A) and 28.5 µm (panel B). Insets show in-plane views of the two bead images. Note that the pixel values are scaled to the maximum dynamic range of the colour tables to allow examination of the spatial features. The average in-plane offset (and SD) of the centroids of the beads were 1.42 ± 0.04 nm (n = 4 beads) at depth of 0 µm and 1.57 ± 0.07 nm (n = 3 beads) at hydrogel depth of 20-30 µm, culminating to an in-plane alignment error of ~ 10% compared to the estimated resolution. Panels C & D illustrate the equivalent comparison for axial alignments (4.7 ± 0.1 nm at 0-µm depth of the hydrogel and 5.9 ± 0.1 nm at 20-30 µm; an error < 13%). Scale bars: 30 nm.

## Legend for supplementary movie

**Supplementary movie: Ca$^{2+}$ spark simulations based on experimentally-mapped positions and phosphorylation states of RyR.** (Left to right): Experimentally-mapped positions and phosphorylation patterns of control and MCT-RV nanodomains, compared with the same RyR positions but with complete dephosphorylation. The upper panels show the cumulative nanodomain's cytoplasmic cleft Ca$^{2+}$ concentration as a function of time. The lower panel shows 2D time lapse dynamics of the local Ca$^{2+}$ concentrations, synchronised with the upper panels.

## References

1. Benoist, D., R. Stones, M. Drinkhill, O. Bernus, and E. White, *Arrhythmogenic Substrate in Hearts of Rats with Monocrotaline-Induced Pulmonary Hypertension and Right Ventricular Hypertrophy*. Am. J. Physiol. Heart Circ. Physiol., 2011. **300**: p. H2230-H2237.
2. McCrossan, Z.A., R. Billeter, and E. White, *Transmural Changes in Size, Contractile and Electrical Properties of Shr Left Ventricular Myocytes During Compensated Hypertrophy*. Cardiovasc Res, 2004. **63**: p. 283-92.
3. Jayasinghe, I., A.H. Clowsley, R. Lin, T. Lutz, C. Harrison, E. Green, D. Baddeley, L. Di Michele, and C. Soeller, *True Molecular Scale Visualization of Variable Clustering Properties of Ryanodine Receptors*. Cell Reports, 2018. **22**: p. 557-567.
4. Jungmann, R., M.S. Avendano, J.B. Woehrstein, M. Dai, W.M. Shih, and P. Yin, *Multiplexed 3d Cellular Super-Resolution Imaging with DNA-Paint and Exchange-Paint*. Nat Methods, 2014. **11**: p. 313-8.
5. Tillberg, P.W., F. Chen, K.D. Piatkevich, Y. Zhao, C.C. Yu, B.P. English, L. Gao, A. Martorell, H.J. Suk, F. Yoshida, E.M. DeGennaro, D.H. Roossien, G. Gong, U. Seneviratne, S.R. Tannenbaum, R. Desimone, D. Cai, and E.S. Boyden, *Protein-Retention Expansion Microscopy of Cells and Tissues Labeled Using Standard Fluorescent Proteins and Antibodies*. Nat Biotechnol, 2016. **34**: p. 987-92.
6. Truckenbrodt, S., M. Maidorn, D. Crzan, H. Wildhagen, S. Kabatas, and S.O. Rizzoli, *X10 Expansion Microscopy Enables 25-Nm Resolution on Conventional Microscopes*. EMBO reports, 2018: p. e45836.
7. Jayasinghe, I.D. and B.S. Launikonis, *Three-Dimensional Reconstruction and Analysis of the Tubular System of Vertebrate Skeletal Muscle*. J Cell Sci, 2013. **126**: p. 4048-58.
8. Tokunaga, M., N. Imamoto, and K. Sakata-Sogawa, *Highly Inclined Thin Illumination Enables Clear Single-Molecule Imaging in Cells*. Nat Methods, 2008. **5**: p. 159-61.
9. Lin, R., A.H. Clowsley, I.D. Jayasinghe, D. Baddeley, and C. Soeller, *Algorithmic Corrections for Localization Microscopy with Scmos Cameras - Characterisation of a Computationally Efficient Localization Approach*. Opt Express, 2017. **25**: p. 11701-11716.
10. Jayasinghe, I.D., D.J. Crossman, C. Soeller, and M.B. Cannell, *A New Twist in Cardiac Muscle: Dislocated and Helicoid Arrangements of Myofibrillar Z-Disks in Mammalian Ventricular Myocytes*. J Mol Cell Cardiol, 2010. **48**: p. 964-71.
11. Soeller, C., I.D. Jayasinghe, P. Li, A.V. Holden, and M.B. Cannell, *Three-Dimensional High-Resolution Imaging of Cardiac Proteins to Construct Models of Intracellular Ca2+ Signalling in Rat Ventricular Myocytes*. Exp Physiol, 2009. **94**: p. 496-508.
12. Cannell, M.B. and C.H.T. Kong, *Quenching the Spark: Termination of Cicr in the Submicroscopic Space of the Dyad*. J Gen Physiol, 2017. **149**: p. 837-845.
13. Sobie, E.A., K.W. Dilly, J. dos Santos Cruz, W.J. Lederer, and M.S. Jafri, *Termination of Cardiac Ca(2+) Sparks: An Investigative Mathematical Model of Calcium-Induced Calcium Release*. Biophys J, 2002. **83**: p. 59-78.
14. Izu, L.T., J.R. Mauban, C.W. Balke, and W.G. Wier, *Large Currents Generate Cardiac Ca2+ Sparks*. Biophys J, 2001. **80**: p. 88-102.
15. Walker, M.A., G.S.B. Williams, T. Kohl, S.E. Lehnart, M.S. Jafri, J.L. Greenstein, W.J. Lederer, and R.L. Winslow, *Superresolution Modeling of Calcium Release in the Heart*. Biophys J, 2014. **107**: p. 3018-3029.

16. Wescott, A.P., M.S. Jafri, W.J. Lederer, and G.S. Williams, *Ryanodine Receptor Sensitivity Governs the Stability and Synchrony of Local Calcium Release During Cardiac Excitation-Contraction Coupling*. J Mol Cell Cardiol, 2016. **92**: p. 82-92.
17. Marx, S.O., S. Reiken, Y. Hisamatsu, T. Jayaraman, D. Burkhoff, N. Rosemblit, and A.R. Marks, *Pka Phosphorylation Dissociates Fkbp12.6 from the Calcium Release Channel (Ryanodine Receptor): Defective Regulation in Failing Hearts*. Cell, 2000. **101**: p. 365-76.
18. Burgoyne, T., E.P. Morris, and P.K. Luther, *Three-Dimensional Structure of Vertebrate Muscle Z-Band: The Small-Square Lattice Z-Band in Rat Cardiac Muscle*. J Mol Biol, 2015. **427**: p. 3527-3537.
19. Luther, P.K., *Three-Dimensional Reconstruction of a Simple Z-Band in Fish Muscle*. J Cell Biol, 1991. **113**: p. 1043-55.